Thermal Image Simulation to Support GNC Testing with PANGU (Paper SIW22-05)

Martin, Iain M.; Dunstan, Martin B.; Vural, Deren; Sanchez Gestido, Manuel

Publication date:
2022

THERMAL IMAGE SIMULATION TO SUPPORT GNC TESTING WITH PANGU

Iain M. Martin[1*], Martin N. Dunstan[1], Deren Vural[1] and Manuel Sanchez Gestido[2], [1]University of Dundee, Dundee, UK, DD1 4HN, [2]ESTEC, ESA, Noordwijk, The Netherlands. *[i.martin@dundee.ac.uk]

Abstract. *Vision-based sensors have been a critical component in a variety of studies to support space applications such as autonomous guidance and landing systems, and orbital maneuvers, with simulated images been shown to be useful to test, calibrate and train these guidance systems. Advances in sensor technology has led to thermal sensors being considered for future autonomous guidance systems because they can provide additional or supplementary information to vision-based systems, leading to a need to provide realistic, simulated thermal images where real data is insufficient. This paper presents recent enhancements to the PANGU software tool to generate simulated thermal images of planets and asteroids from lunar surface thermal models and orbiting spacecraft using thermal balance equations.*

Introduction. Image simulation of planetary surfaces, asteroids and spacecraft has been used to support the development, testing and calibration of autonomous guidance systems for a wide variety of space applications through simulating the onboard navigation sensors. Vision and LiDAR sensors have most commonly been considered and these have been tested, validated and calibrated using a variety of real images, synthetic (simulated) images and flight tests on Earth. With advances in the technologies, thermal (infrared or near-infrared) sensors are now being considered to enhance GNC (Guidance, Navigation and Control) systems for future missions to provide additional information to traditional vision-based systems.

PANGU. PANGU (Planet and Asteroid Natural scene Generation Utility) is an established software tool designed to generate simulated visual and LiDAR images of planetary surfaces, small bodies, spacecraft and surface rovers. PANGU models are created by importing real data such as shape models or DEMs (Digital Elevation Models) and enhancing them through the addition of synthetic terrain and small-scale features to increase the resolution, where required, with representative terrain features [1]. Simulated images are then generated with the integrated visual and LiDAR renderer which includes a built-in, customizable GPU-based camera model to simulate camera noise, distortion and other effects to be applied in real-time for image generation to support both open and closed loop testing.

Thermal Images. Simulating thermal images presents a significant additional challenge to visual images because the process of surface heat emission and absorption is more complex than light-surface interactions which can be modeled through BRDFs (Bidirectional Reflectance Distribution Function) and may include time-based effects. The thermal response is determined by the surface material properties (e.g., thermal inertia, emissivity and absorptivity) and the energy flux and can change with time.

Existing work. Commercial thermal engineering tools using Finite Element or Finite Difference analysis techniques to converge to a steady state solution (e.g., ESATAN [2]) are well established but are limited to working with simplified, low-resolution mesh models in order to simulate and manage the heat-transfer within a craft and are not designed to simulate high-resolution thermal radiance images of spacecraft surfaces from complex mesh models.

There is a small body of work simulating thermal images of aircraft [3], [4] in atmospheric conditions from which we can extend concepts such as using thermal balance equations and a radiometric Look-Up-Table (LUT) with pre-calculations, but this work is not directly applicable to either in-orbit or planetary lander scenarios on airless bodies such as the Moon and asteroids.

Available data. For thermal imaging data of planetary surfaces, the most significant resources are the NASA Diviner dataset from the LRO (Lunar Reconnaissance Orbiter) spacecraft which has provided a large data set of thermal images [5], from which thermal models of the lunar surface have been derived which we use in our work. The Diviner data set has a resolution approximately 128 pixels per degree. The Hayabusa-2 mission contained a thermal sensor from which thermal radiance and false-colour temperature images of asteroid Ryugu are publicly available, so we have used them for comparison and validation to our simulated images. The OSIRIS-REx mission is also expected to provide a dataset of thermal images in the next few years.

Thermal simulations of planetary surfaces.

From the temperature models derived from the Diviner data, the temperature measurements of the Moon during a day-night period can be observed to show a distinctive pattern for the non-polar regions as shown in *Fig. 1*, which is a representation of graphs presented by Vasavada [6]. The graph shows the temperatures measured by the Diviner instrument as a function of time of day in hours from noon at three different latitudes. The maximum temperature is at local noon falling off towards sunset. During the night, temperatures fall almost linearly with a smooth transition at sunset and sunrise. The temperature rises rapidly during the morning until the next noon. On a global scale, the regolith properties are shown to be uniform. Areas surrounding fresh crater ejecta show higher thermal inertia than regions with older craters. Cold spots have been observed around recent small craters and very rocky regions also show an increase in thermal inertia. Large individual rocks can

show up as warm spots because they can cool down at a slower rate in the night than their surrounding regolith.

This temperature model was added to PANGU in the form of a diurnal and seasonal temperature LUT which enables a base temperature of any point on the surface of the Moon to be estimated from the effective latitude, defined as the local surface normal angle relative to the rotation axis, and the effective time of day, defined as the local surface normal angle relative to the Sun direction. The emitted radiance in each detector channel is then calculated from the temperature of the surface and emissivity which is parameterizable as a material property. This is added to the reflected radiance in each channel, defined by a BRDF. Additional refinements include accounting for seasonal effects in the polar regions, global surface material properties, thermal inertia and effective absorptivity, and local variations in emissivity and absorptivity.

Evaluation of this thermal model was performed though comparison of PANGU simulated thermal images with Clementine LWIR lunar images and Hyabus 2 images of asteroid Ryugu. An example Clementine/PANGU image comparison is shown in *Fig. 2*, LLA020A.034 at 85.67°S latitude, 4.8° longitude, obtained on timestamp 1994-02-27T07:06:54.314Z. The Clementine image contained bright fixed-pattern noise which obscures the details so was de-speckled and equalized.

The PANGU model for this comparison was created from a Kaguya DEM, with the Clementine SPICE kernels used to obtain the image position, attitude and lighting conditions to generate the comparison image. The histogram comparison in *Fig. 3* shows a reasonable match, considering the low resolution and noise in the original image.

Small bodies. There was no equivalent thermal model available for a small body but as most asteroids are rocky airless bodies, it is not unreasonable to make an initial assumption that their temperature profiles could follow a similar day/night profile as the Moon, with different maximum and minimum temperatures. For this work, our approach was to apply the lunar thermal model to a shape model of asteroid Ryugu, using the known minimum and maximum temperatures for Ryugu, then evaluate the results though comparison to Hayabusa thermal images. An example from this evaluation is shown in *Fig. 4* with a histogram of the two images shown in *Fig. 5*. An emissivity map of Ryugu was not available so local emissivity variations were estimated from the images to demonstrate the concept.

Thermal Simulations of spacecraft. Simulating thermal images from an orbiting spacecraft or satellite presents additional challenges and the LUT-type model is unlikely to be sufficiently realistic. The most significant heat source is still likely to be direct solar but spacecraft are probably orbiting a planet which will contribute significant amounts of emitted thermal radiance and reflected solar radiance. The spacecraft itself may contain radiators for heat management and most surfaces will be covered in different types of material such as Multi-Layer Insulation (MLI), reflectors and radiators. For our initial version, we assume that the majority of the external surfaces are covered by MLI material and the external surfaces respond instantly to changes in the flux, so conduction is not a significant effect. We acknowledge that this assumption is likely to only apply to heavily insulated surface materials such as those covered in MLI.

Thermal balance equations. The theoretical temperatures of a spacecraft can be modelled using thermal balance equations [8]. The contributions of direct solar radiation, reflected solar radiation, planetary emission, background heat and internal heat dissipating radiators enable temperatures of spacecraft surfaces to be calculated.

Thermal contributions. The reflected radiation from a nearby planet (e.g., the Earth) is scaled by the visibility factor (i.e., the visible area of the planet) and the local time of day to approximate the incoming solar contribution. The planetary radiation is defined at the surface of the Earth and scaled by the inverse square law over the orbital radius.

The planetary emission model includes a 218K black body contribution from the upper atmosphere, and 288K black body contribution from the surface The fourth power of the temperature is related to the sum of the heat sources at a surface as shown in *Eqn. 1* as defined by Savage [8].

$$\boldsymbol{T^4} = \boldsymbol{Q}_{\text{back}} + \boldsymbol{Q}_{\text{solar}} + \boldsymbol{Q}_{\text{albedo}} + \boldsymbol{Q}_{\text{planet}} + \boldsymbol{Q}_{\text{internal}}$$

The individual contributions are defined as:

- Background heat (Q_{back}),
- Direct solar (Q_{solar}),
- Reflected solar (Q_{albedo}),
- Planetary emission (Q_{planet}), and
- Internal heat sources or sinks.

The background heat term is used approximate the background temperature for the simulation, i.e. this could be 3K for the Cosmic Microwave Background 3K or 300K for laboratory room temperature.

The direct solar contribution is modelled as:

$$\boldsymbol{Q}_{\text{solar}} = \left(\frac{J_s \boldsymbol{A}_{\text{solar}}}{\sigma \boldsymbol{A}_{\text{surface}}}\right) \cdot \mathbf{max}(\mathbf{N} \cdot \mathbf{L}_{\text{sun}}, \mathbf{0}) \cdot \mathbf{S}_{\text{shadow}} \cdot \left(\frac{\boldsymbol{\alpha}_{\text{VIS}}}{\boldsymbol{\varepsilon}}\right),$$

where:

- J_s, is the solar flux, scaled by the inverse square law: Sun distance vs 1A.U.
- $A_{solar}/A_{surface}$ is the absorption area relative to emittance area ratio,
- σ is the Stefan-Boltzmann's constant
- L_{planet} is the direction to each sample,

- The dot product is the cosine foreshortening term for the local surface normal N relative to the Sun direction,
- The S_{shadow} term represents the local shadow factor for the point of interest (0=shadowed, 1=lit), and
- α/ε represents the effective absorptivity ratio defined for sources peaking in the visual band (i.e. the Sun).

Similar equations are defined for reflected solar (Q_{solar}) and planetary emission (Q_{planet}). The reflected solar term is more complex to implement because integrating the reflected albedo across the visible surface of the planet for arbitrary altitudes and surface normal directions would not feasible for our real-time rendering approach. Instead, we approximation the reflected solar contribution by sampling the reflected albedo at a number of points across the surface of the disk that would potentially be visible to any point of the spacecraft. The planetary emission can be considered to be a constant source at the surface of the planet. The inverse square law and the local surface normal direction will cause variations in the emission received by the surface. In addition, we include the facility to include heaters in the models to simulate heat dissipation such as for radiators.

Initial validation of the stateless model for spacecraft was performed using the validated ESATAN Thermal Modelling Suite (TMS) tool. This is a finite element/finite difference solver that can be used for spacecraft thermal management calculations and so can be used to obtain temperature values with which to validate PANGU thermal simulations. ESATAN is not designed to generate high-resolution thermal radiance images model complexity is limited, so only temperature values are compared and not images.

Equivalent PANGU and ESATAN CubeSat models were created with the same material parameters used to define the dual-bulk MLI coating and identical orbits were defined to simulate a CubeSat orbiting the Earth. The temperature results are sampled at single degree intervals for the complete orbit on each face of the cube. A temperature plot from the +y plot is shown in *Fig. 6*. In general, the plots show a reasonable match with some difference in the reflected solar contribution mainly which we believe could be due to insufficient sampling.

This stateless approach allows fast rendering of complex models with temperatures calculated for each vertex in the model. At the pixel level, these temperatures can either be used to generate false-color temperature images or converted into thermal radiance values using Planck's law and local variations in thermal emissivity. An example of a PANGU rendered spacecraft model is shown in *Fig. 7*. as both a thermal radiance image and a false color image.

Future work is planned to refine and further validate the thermal simulations using more complex models in ESATAN and through simulation and comparison of thermal spacecraft images should they and their associated model and metadate become available. In addition, experimental work is being developed to simulate time-based effects to model conduction.

Acknowledgements: PANGU was developed by the University of Dundee for ESA and is being used on many European activities aimed at producing precise, robust planetary lander and rover guidance systems.

References.

[1] I. Martin, S. Parkes, M. Dunstan, M. Sanchez Gestido, G. Ortega, "Simulating planetary approach and landing to test and verify autonomous navigation and guidance systems", ESA GNC 2017, Salzburg, May 29th–June 2nd, 2017.

[2] ESATAN, https://www.esatan-tms.com. Accessed 26/06/2022.

[3] X. Huang, et al., "GPU-based high-precision real-time radiometric rendering for IR scene generation, Infrared Physics and Technology", Vol. 65, pp.134–143, 2014.

[4] N. Li, et al., "A real-time infrared imaging simulation method with physical effects modeling of infrared sensors", .Infrared Physics & Technology, Vol. 78, pp45–57, 2016.

[5] Diviner data, https://www.diviner.ucla.edu/single-post/2018/04/20/New-Diviner-Level-4-Data-Products. Accessed 26/05/2022.

[6] A. R. Vasavada et al. "Lunar equatorial surface temperatures and regolith properties from the Diviner Lunar Radiometer Experiment. Journal of Geophysical Research E: Planets", 2012.

[7] J. P. Williams et al., "The global surface temperatures of the Moon as measured by the Diviner Lunar Radiometer Experiment", Vol 283, pp. 300–325, Feb 2017.

[8] C. J. Savage, "Spacecraft Systems Engineering (3rd Ed)", chapter 11 "Thermal control of spacecraft", Wiley.

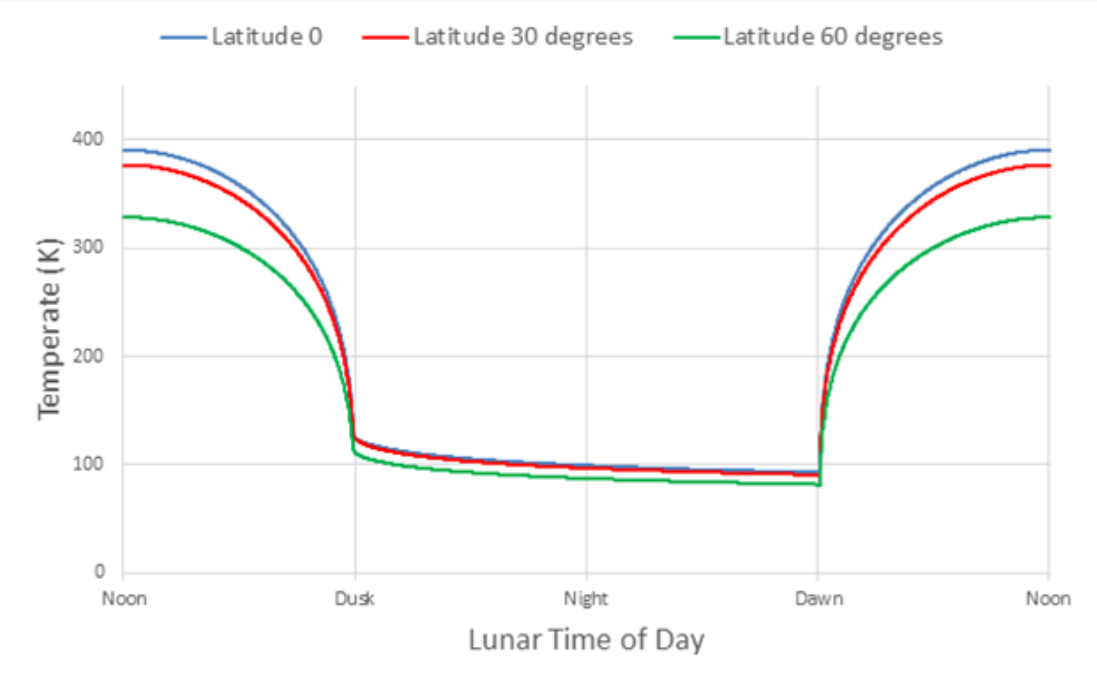

Figure 1: Model of lunar surface temperature variations by latitude

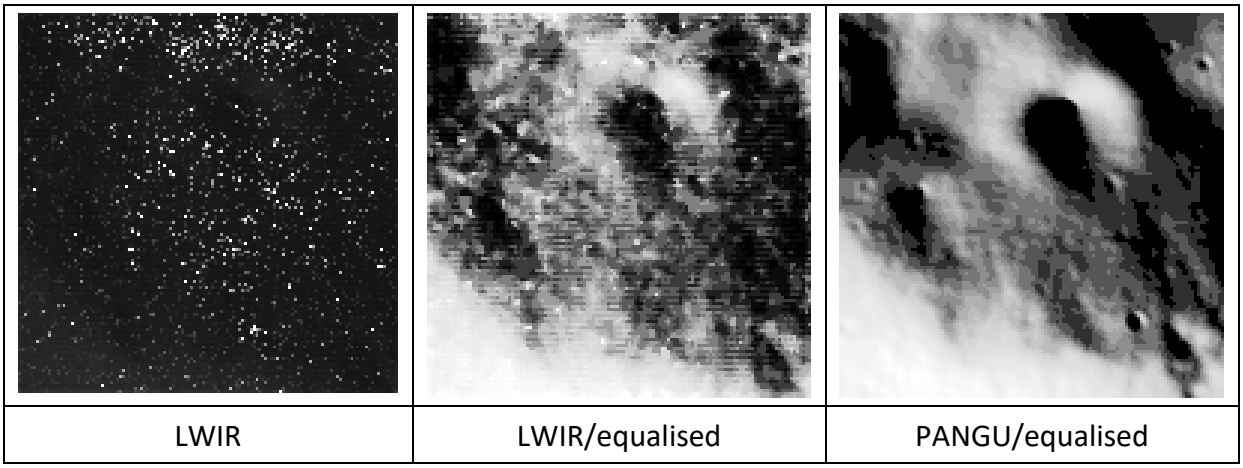

LWIR	LWIR/equalised	PANGU/equalised

Figure 2: Clementine image LLA020A.034 and the PANGU simulated equivalent

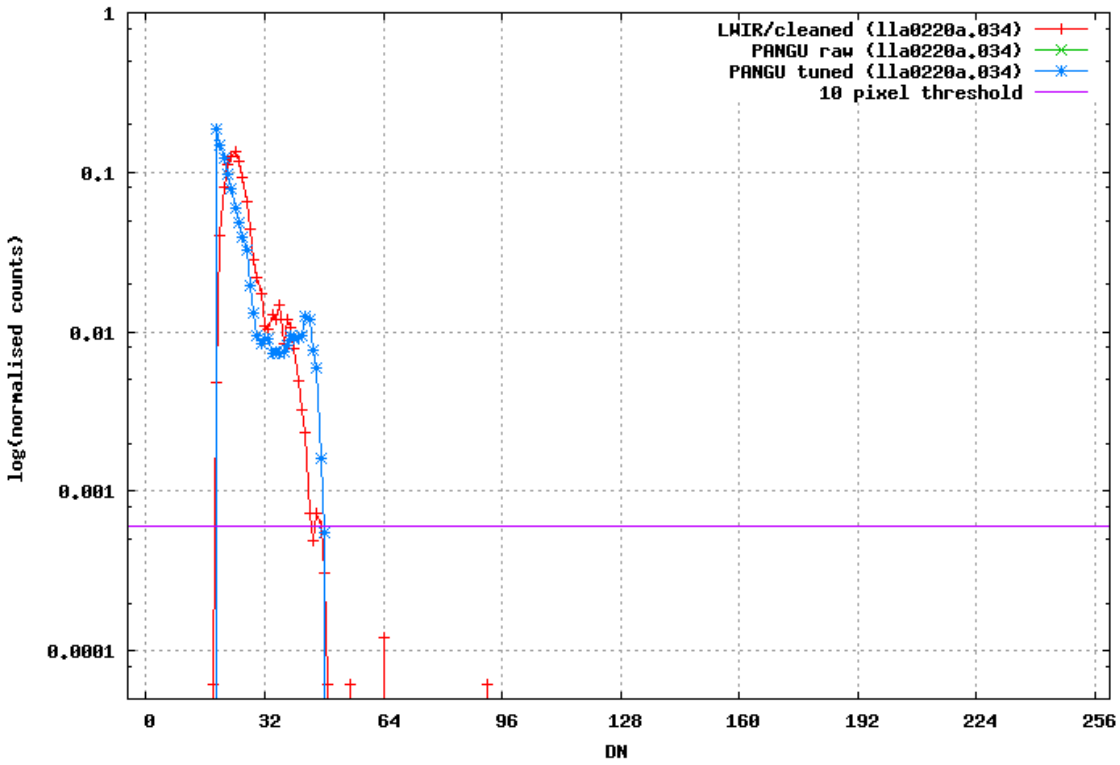

Figure 3: Grey-level histogram of the LWIR and PANGU images

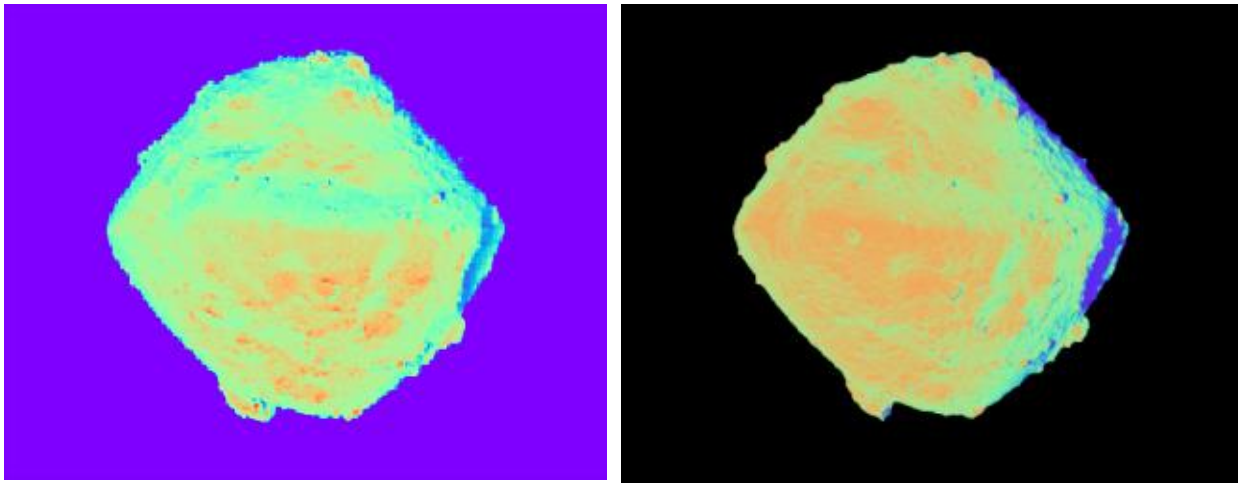

Figure 4: Hayabusa2/TIR temperature image 2018-08-01@17:47:44 (L) and PANGU simulation (R)

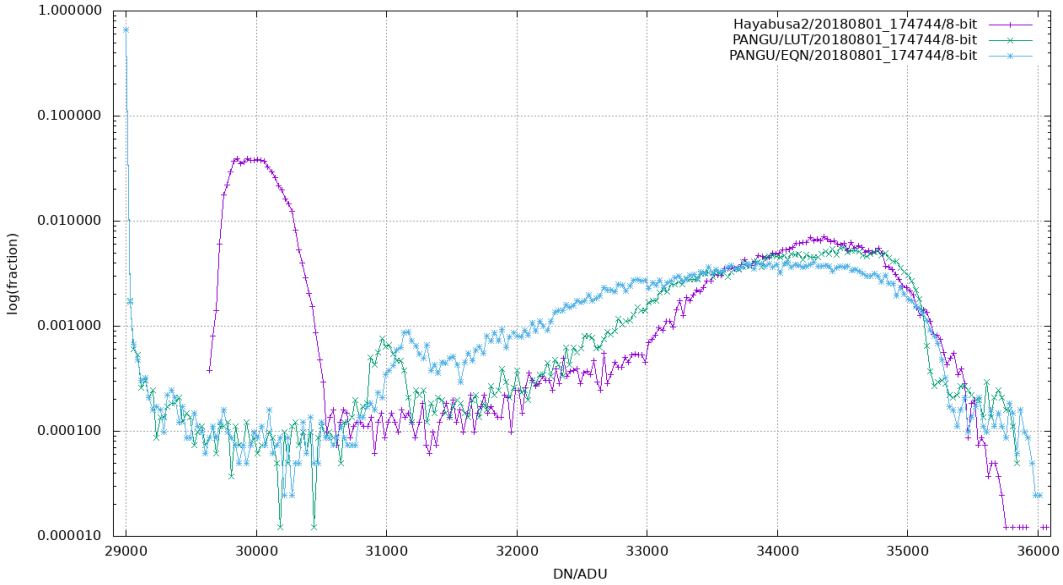

Figure 5: Histograms of thermal radiance images: Hayabusa 2 TIR, PANGU LUT and PANGU equations

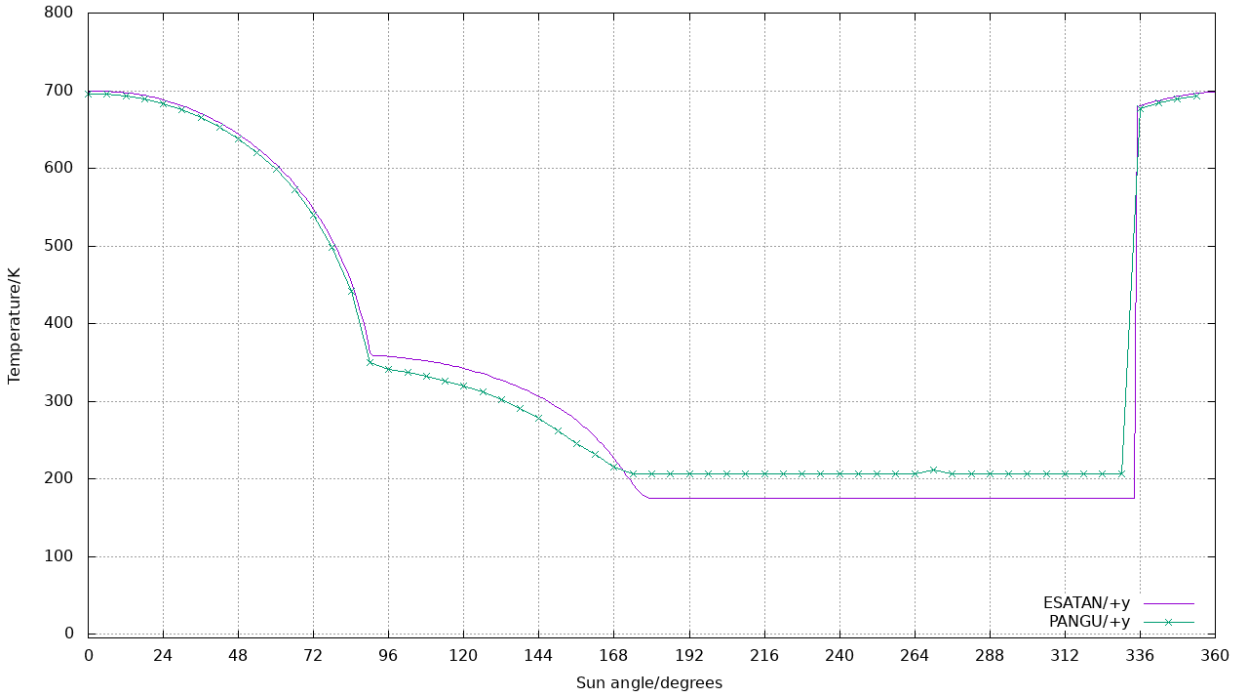

Figure 6: PANGU vs ESATAN MLI CubeSat temperature for face +y

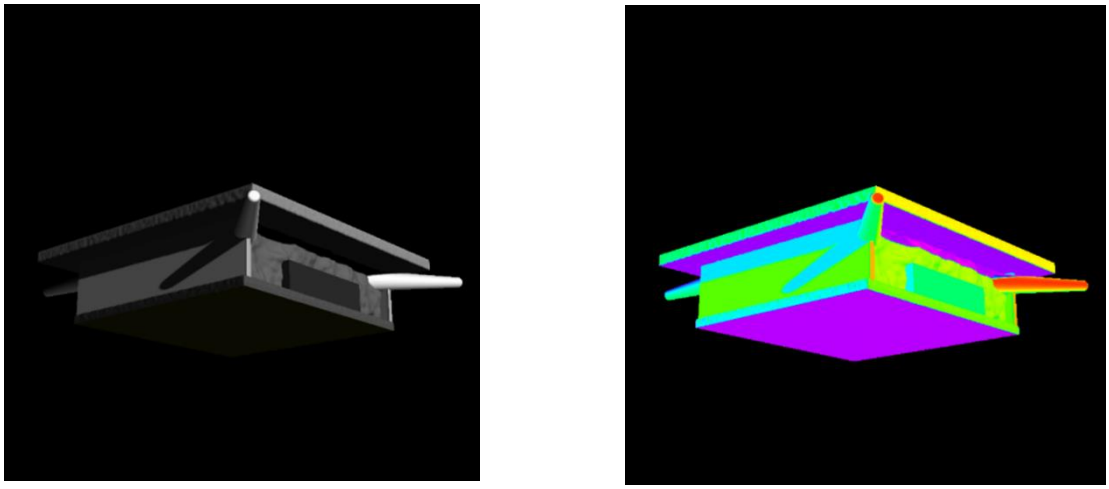

Figure 7: PANGU thermal radiance simulated image of a spacecraft model (left) and the false color temperature (right)